SCIENTIFIC REPORTS

natureresearch

Check for updates

OPEN

Ultrafast reprogrammable multifunctional vanadium-dioxide-assisted metasurface for dynamic THz wavefront engineering

Javad Shabanpour✉, Sina Beyraghi & Ahmad Cheldavi

In this paper, for the first time, a new generation of ultrafast reprogrammable multi-mission bias encoded metasurface is proposed for dynamic terahertz wavefront engineering by employing VO2 reversible and fast monoclinic to tetragonal phase transition. The multi-functionality of our designed VO2 based coding metasurface (VBCM) was guaranteed by elaborately designed meta-atom comprising three-patterned VO2 thin films whose operational statuses can be dynamically tuned among four states of "00"-"11" by merely changing the biasing voltage controlled by an external Field-programmable gate array platform. Capitalizing on such meta-atom design and by driving VBCM with different spiral-like and spiral-parabola-like coding sequences, single vortex beam and focused vortex beam with interchangeable orbital angular momentum modes were satisfactorily generated respectively. Additionally, by adopting superposition theorem and convolution operation, symmetric/asymmetric multiple beams and arbitrarily-oriented multiple vortex beams in pre-demined directions with different topological charges are realized. Several illustrative examples successfully have clarified that the proposed VBCM is a promising candidate for solving crucial terahertz challenges such as high data rate wireless communication where ultrafast switching between several missions is required.

In recent years, the scope of THz science and technologies has reached a maturity and attracted massive attention due to their potential applications like biomedicine[1], security checking and high data rate transmit through wireless communication[2–4]. However, as the key technique, manipulating EM waves reveals the necessity of employing metasurfaces as the two-dimensional analogous of more general volumetric metamaterials to furnish an inspiring groundwork for realizing some rich diverse applications such as, but not limited to, invisibility cloaks[5,6], negative refraction[7], optical illusion[8] and epsilon near zero behaviors[9,10].

Recently, T. Cui *et al.* has revolutionary introduced the concept of digital metasurfaces as a link between the physical and digital worlds, making it possible to revisit metamaterials from the viewpoint of information science where manipulation of EM waves with different functionalities can be realized by controlling sequences of digital coding states "0" and "1" with opposite phase responses[11]. Due to the lower weight and being easier to design and fabricate, digital metasurfaces have experienced rapid development compared to traditional wave manipulation[12]. By purposefully distributing coding particles over a 2D plane in a periodic or aperiodic manner, a variety of exquisite physics phenomena and innovative EM devices have been created[13–17].

However, in most of these strategies, the metasurfaces are designed for a specific application and their functionalities remain fixed once they are constructed. For example, Shao *et al.* proposed a dielectric 2-bit coding metasurface with distinct functionalities from anomalous reflection to vortex beam generation[18]. Dual-band 2-bit coding metasurface to fully control vortex beams carrying orbital angular momentum with different topological charges (*l*) was discussed in ref. [19], But the lack of adjustability significantly hinders their practical applications.

Owing to the increasing need for system integration, a single metasurface that possesses multiple diversified functionalities in a real-time manner with tunable meta-atoms is highly desired notably at THz frequencies[20–22]. Programmable digital metasurfaces significantly furnish a wider range of wave-matter functionalities which renders them especially appealing in the applications of imaging[23,24], intelligent structures[25–27] and wireless communications[28–32]. More recently, the concept of space-time digital metasurface has been raised to obtain

Department of Electrical Engineering, Iran University of Science and Technology, Narmak, Tehran, 16486-13114, Iran. ✉e-mail: m.javadshabanpour1372@gmail.com

simultaneous manipulations of EM waves in both space and frequency domains which substantially expand the application scope of digital metamaterials[33–36]. Until the present, some papers have brought forward electronically tunable coding metasurfaces in microwave frequency by using pin diodes in each coding element[24,37,38]. For example, Huang *et al*. presented a method to design a 2-bit digitally-controlled coding metasurface in order to realize different far-field patterns. By integrating two pin diodes in each coding particles and switching their operating states, producing four phases responses was realized[39]. In light of the complexity and lack of commercial access of active elements (pin or varactor diodes) at high frequencies, scaling these devices to THz regime is very difficult if not impossible[40].

For real-time manipulating THz waves, an efficient technique is to integrate standard metasurface with phase-change materials (PCM), for instance, graphene[41–43], liquid crystal[44–47], GST[48,49] and vanadium dioxide (VO2)[50–53]. To implement such a platform, we have benefited from VO2 exotic properties. VO2 is a smart material, that undergoes an ultrafast and brutal reversible first-order phase transition from insulating monoclinic ($P2_1/c$) to the metallic tetragonal ($P4_2/mnm$) phase, above critical temperature $T_c = 68$ °C[53]. Since the critical temperature is a function of V-V distance in crystal structure, decreasing in critical temperature would be feasible by adopting doping technique[54,55]. This metal-insulator transition (MIT) can be provoked by thermal[56,57], optical[58–60] or electrical (charge injection or Joule heating)[61,62] stimuli. The origin of such an insulator to metal transition is still under debate[63–65]. This transition in VO2 can occur within an order of several nanoseconds or even in picoseconds range for optical activation[66]. The VO2 phase alternation that was studied in ref. [67] and ref. [68] through time-resolved x-ray diffraction and time-resolved optical transmission respectively, revealed that only a short time ($<500\,fs$) was required for taking place the MIT. Moreover, Cavalleri's study indicated that the photo-induced transition time for VO2 thin film (50 nm) could reach 80 fs[69].

Electrical and optical property of VO2 has dramatic changes (4 to 5 order of magnitude change of the electrical conductivity) across the two phases[70]. Owing to the ultrafast transition duration, almost near room critical temperature and fruitful structural transition behaviors, VO2 has became a striking material in tunable metamaterial devices at GHz[71,72], optics[73–75] and has numerous fantastic applications in THz frequencies such as reconfigurable THz filters[76,77], polarization converter[78–82], reflection/transmission THz waves modulator[83–85], tunable THz absorbers[86,87] and reconfigurable antennas[88,89]. In 2016, a simple VO2-assisted digital metasurface was proposed to dynamically control the near-infrared light[90]. By allowing voltage to be locally applied to the VO2 and distributing unit cells in one direction, switchable beam splitters with only limited splitting angles have been realized. Regarding that the reflection phase of the proposed structure is either 0° or 180° relying on the state of VO2, several basic functionalities and fundamental THz challenges such as anomalous reflection, multi-beams and vortex beam generation with adjustable properties are not accessible with this structure.

In departure from the abovementioned work, wherein the mission of utilizing VO2 in the structure is limited to only a single tunable function, we present, to the best of author's knowledge, the first VO2-based coding metasurface (VBCM) that can be reprogrammed for realizing multi-type functionalities from vortex beams with different topological charges toward emitting multiple arbitrarily-oriented pencil beams. Although, some articles have reported graphene-based coding metasurface for real-time manipulation of THz waves recently, but the graphene is of great loss compared to VO2. Graphene consists only of a monolayer of carbon atoms compared to volumetric VO2 and its switching time is thousands of times slower than VO2. Disadvantages such as difficult fabrication process and very low switching time, made graphene to be impractical in real-time wave manipulation meta-devices[90,91].

Although today's applications in THz regime as high data rate wireless communication and ultra-massive MIMO communication are in dire need of ultrafast THz wavefront manipulation, we are not aware of any reports of ultrafast real-time THz wavefront engineering and this field is still largely unexplored and we believe that our proposed ultrafast VBCM structure has the great potentials to fill this gap.

In this paper, an ultrafast versatile 2-bit VO2-based coding metasurface with programmable meta atoms is designed whose operational statuses can be dynamically switched between four states of "00", "01", "10", and "11". By applying external bias voltage controlled by an FPGA platform to the elaborately designed meta-atom, the capability of manipulating THz wavefront in a real-time manner has been achieved. Each constitutive unit-cell of the VBCM integrates three-patterned VO2 layers fed by two biasing voltages (ON/OFF), therefore it can alterably possess four reflection phase responses of 0, $\pi/2$, π, and $3\pi/2$ without changing the geometrical parameters. In order to expose the capacities of our structure in multifunctional wavefront engineering, we have arranged various coding samples to accomplish different interchangeable functions from vortex beams generation with different OAM modes toward emitting multiple arbitrarily-oriented pencil beams without re-optimizing or re-fabricating the structure. By adopting convolution and superposition theorems on the far-field pattern, several THz fundamental challenges such as symmetric/asymmetric multiple pencil beams and arbitrarily-oriented multiple vortex beams with different OAM modes, with ultrafast switching time are solved by our proposed VBCM structure. The presented concepts have been confirmed through a number of numerical simulations and theoretical predictions. To the best of our insight, this is the first ultrafast re-programmable coding metasurface based on VO2 phase transition that armed a platform for realizing some rich interchangeable missions at THz frequencies. The authors believe that the proposed VBCM paves the way for ultrafast multifunctional THz wavefront engineering and future practical applications.

Results

Design of the switchable multifunctional VBCM. Figure 1 represents the basic meta-atom of the VO2 integrated metasurface composing of three layers, which, from top to bottom, are the VO2 layers, dielectric substrate, and a gold plane to impede the transmission energy into the back of the VBCM. At the top layer, three patterned VO2 layers deposited on the sapphire as the suitable substrate ($\varepsilon_r = 9.4$. $\tan\delta = 0.0001$) with the
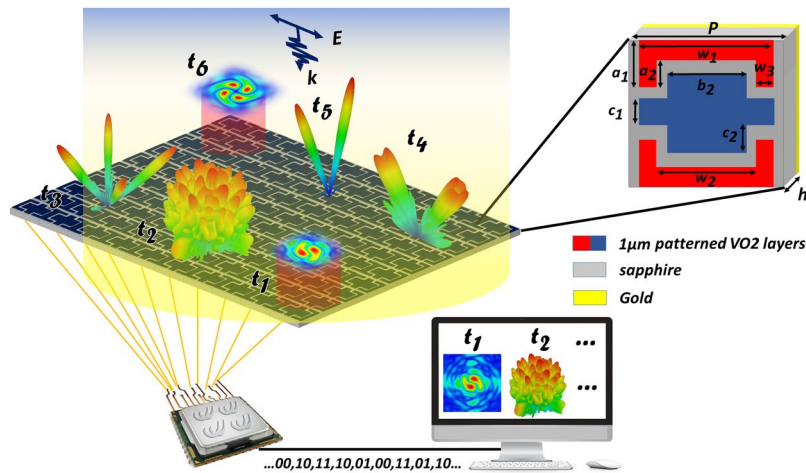
Figure 1. Sketch representation of reprogrammable VO2 based coding metasurface controlled by an FPGA platform. Different spatial coding patterns can be encoded onto the structure simultaneously through computer-programmed biasing network at distinct moments of t_1, t_2, t_3 ….

thickness of $h = 38 \ \mu m$. Up to now, VO2 thin films have been prepared on different substrates as silica glass[92], polyimide[79,91], silicon[93–95] and sapphire[76,96,97] by several techniques from chemical vapor deposition[98] to reactive electron-beam evaporation[99], but it is preferable to use sapphire substrate to reach high-quality VO2 thin films due to the beneficial lattice matching effect[100].

The complex dielectric properties of the VO2 can be characterized by the Bruggeman effective-medium theory in the THz range, wherein, ε_d and ε_m denotes the dielectric constant of the semiconductor and metallic regions respectively and V represents the volume fraction of metallic regions[78].

$$\varepsilon_{VO_2} = \frac{1}{4}\left\{ \varepsilon_d(2 - 3V) + \varepsilon_m(3V - 1) \right.$$
$$\left. + \sqrt{[\varepsilon_d(2 - 3V) + \varepsilon_m(3V - 1)]^2 + 8\varepsilon_m\varepsilon_d} \right\} \tag{1}$$

At room temperature the dielectric constant of VO2 is about 9 in the insulting state[79,82,101,102] and by applying external bias voltage directly to VO2 thin film, the structural transformation occurs and VO2 turns into the rutile phase. Typical VO2 films that are grown on c-type or r-type sapphire substrate, display electrical conductivity in the range of 10~100 S/m in insulating state and as high as an order of 10^5 S/m in the metallic state[76]. Frequency independent conductivity of VO2 is set to be $\sigma = 10 \ S/m$ (OFF state)[92,103] and $\sigma = 5 \times 10^5 \ S/m$ (ON state)[62,80,104] in the insulating and metallic phase corresponding to $T_c = 300 \ K$ and $T_h = 400 \ K$ respectively. The periodicity of our subwavelength meta-atoms is $P = 100 \ \mu m$. The other geometrical parameters are $W_1 = 90 \ \mu m$, $W_2 = 62 \ \mu m$, $W_3 = 14 \ \mu m$, $a_1 = 39 \ \mu m$, $a_2 = 26 \ \mu m$, $b_1 = 90 \ \mu m$, $b_2 = 52 \ \mu m$, $b_3 = 19 \ \mu m$, $c_1 = 14 \ \mu m$, $c_2 = 26 \ \mu m$ respectively. The thickness of VO2 films is assumed to be $t = 1 \ \mu m$. All of these geometrical dimensions are extracted from an extensive simulation and optimization process to obtain four reflection phases of 0, $\pi/2$, π, and $3\pi/2$ (phase step of 90°) to mimic four digital states of "00", "01", "10", "11" and any change in dimensions will worsen this phase differences. Contrary to geometrically encoded metasurface, the employed meta-atoms of the VBCM structure in this study have the same dimensions but with different properly bias voltages leading to call this structure as bias-encoded metasurface. All the numerical simulations are carried out by means of Commercial software CST Microwave Studio. For evaluating the reflection characteristics for the infinite array of digital elements, open (add space) boundary condition is applied along z-axis whilst periodic boundary conditions are utilized along the x- and y-directions to incorporate the mutual coupling effect between neighboring elements. The simulated reflection spectra are depicted in Fig. 2(a,b) for different sets of external bias voltage. It is clearly observed from Fig. 2(b) that with appropriately biasing three patterned VO2 layers from top to bottom as follows: ("OFF/OFF/OFF", "ON/ON/ON", "ON/OFF/ON" and "OFF/ON/OFF"), our elaborately designed meta-particle has been successful in providing a phase step of 90° at 0.44 THz. Also, the reflection amplitudes are above 0.82 which means that the meta-atom non-absorptive behavior has been achieved. We have deliberately selected these two temperature points since VO2 at these two points is in the dielectric or metallic steady-state phases[90]. Furthermore, the Ohmic loss of the meta-atom is maximum at intermediate temperatures which leads to a sharp drop in the reflection amplitude which makes device efficiency to be minimized. It is worth mentioning that to maintain the symmetry of the simulation results, both top and bottom VO2 layers (red colors in Fig. 1) must be geometrically identical and switched "ON" and "OFF" simultaneously. Finally considering the abovementioned constraints and avoiding VO2 intermediate phases, employing three- patterned VO2 layers in the meta-particle that leads to the complexity of the biasing system is forced to users. It can be found from Fig. 2(b) that the perfect 2-bit characteristic occurs at 0.44 THz which means that the approximate size of our subwavelength meta-atoms equals $\lambda/7$.
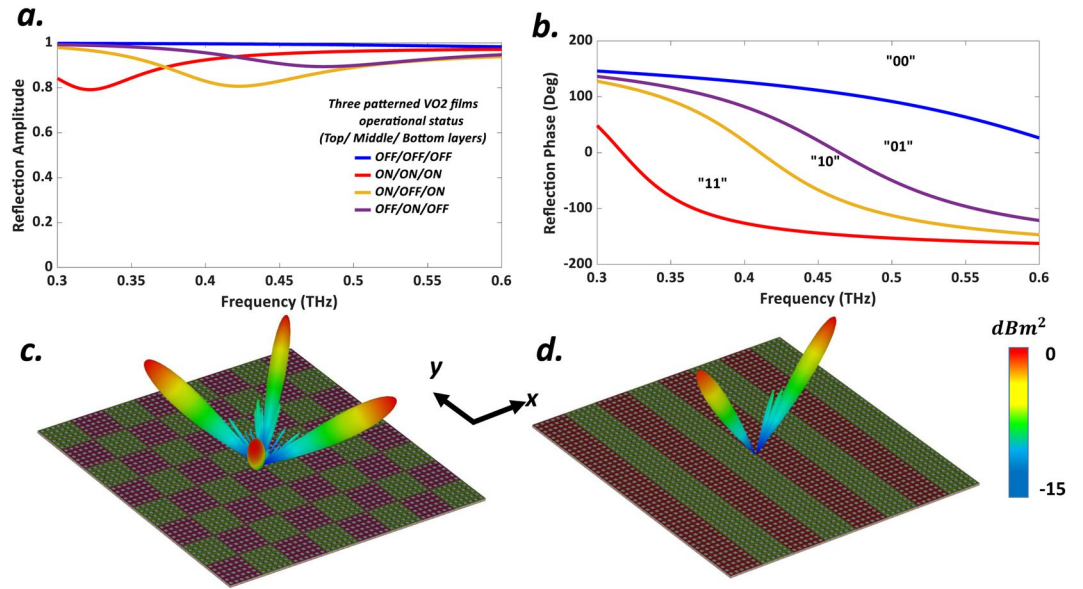
Figure 2. Simulated reflection spectra (**a**) amplitude and (**b**) phase of VO2 based meta-atom under illuminating y-polarized normal incident plane wave. The simulated 3D far-field pattern results at 0.44 THz by adopting only digital elements of "00" and "10" with 180° phase difference (**c**) VBCM structure encoded by [00, 10, 00, 10 …/10, 00, 10, 00 …] (**d**) VBCM driven by [00, 10, 00, 10 …/00, 10, 00, 10 …].

Meanwhile, a maximum phase range of 260° is attained here that is wide enough for acceptable functioning of our ultrafast multifunctional VBCM for real-time THz wavefront engineering.

Before beginning the next section, it is worthwhile mentioning that the multi-functionality of the VBCM structure can be realized when external dc bias voltage/current is applied to each individual unit-cell independently through the Au electrodes deposited on the top of the patterned VO2 layers to form a good Ohmic contact. The main mechanism for this voltage/current driven MIT process remains controversial as it may originate from Joule heating[61,105] or electric field effects[106,107]. Recently the viewpoint of Zimmers et al.[61], was that the local Joule heating plays a predominant role in the dc voltage (or DC current) induced MIT. Wu et al.[106] claim that the Joule heating effect was negligible and the electric field alone is sufficient to induce MIT. Beyond these two competing claims, some papers were commented that these two main mechanisms are considered to be mixed and were difficult to disentangle these two effects in the VO2 voltage-driven MIT process[108,109].

To minimize the EM coupling between the adjacent meta-particles, the VBCM structure comprises of $N \times N$ array of $M \times M$ identical subwavelength unit-cells that constructs the so-called super-unit cell or lattices. The length of one lattice is MP and the length of the whole VBCM is equaled to NMP. The metasurface is assumed to be illuminated by a y-polarized normal incident plane wave throughout the paper. From the well-known antenna theory, the far-field scattering pattern function of the VBCM can be expressed by[11]:

$$E_{scat}(\theta, \varphi) = E_{elem}(\theta, \varphi) \times F(\theta, \varphi) \qquad (2)$$

$$F(\theta, \varphi) = \sum_{m=1}^{N} \sum_{n=1}^{N} a_{mn} \exp\left(-j\left\{\varphi(m, n) + kp\sin\theta\left[\left(m - \frac{1}{2}\right)\cos\varphi + \left(n - \frac{1}{2}\right)\sin\varphi\right]\right\}\right) \qquad (3)$$

in the above equations, θ and φ are the elevation and azimuth angles of the desired direction, P demonstrates the period of lattice along both x- and y-directions, a_{mn} and φ_{mn} are the demonstrator of reflection amplitude and phase of each lattices respectively and $k = 2\pi/\lambda$ where λ is a working wavelength. Establishing a 2D inverse fast Fourier transform (2D-IFFT) to accelerate the calculation make this formula beneficial for the prediction of scattering patterns caused by different coding sequences. The VBCM structure occupied with 8×8 array of 6×6 identical unit-cells throughout this study. In the two next layouts, only digital elements of "00" and "10" with 180° phase difference are adopted. By distributing these two digital elements in alternate rows or columns, the reflected wave is split into two symmetrically oriented scattered beams ($\theta = 34°$, $\varphi = 0°$, 180°) governed by generalized Snell's law[110] as shown in Fig. 2(d). By arranging the above two digital elements in a chessboard configuration (see Fig. 2(c)), the incoming energy redirected into four scattered main beams of ($\theta = 53°$, $\varphi = 45°$, 135°, 225°, 315°) at 0.44 THz that have an excellent conformity with the theoretical predictions. According to generalized Snell's law, with increasing the observation frequency, the reflection beams come closer to the boresight direction[111].

Phase-gradient Coding Sequence: anomalous reflection. 1-bit coding metasurface is not capable of producing an arbitrary tailored single reflected beam as an exciting example of THz wavefront engineering. By extending the concept, our 2-bit VBCM structure has greater freedom to manipulate EM waves, for instance,
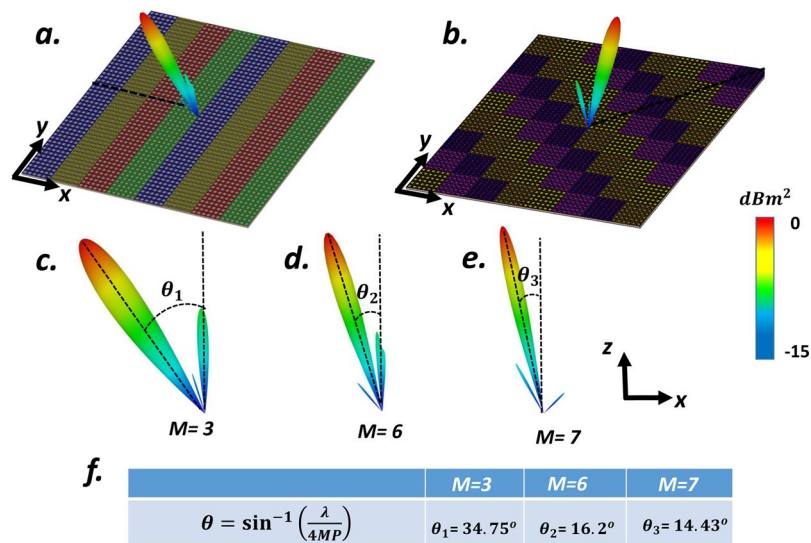
Figure 3. 3D far-field scattering pattern of anomalous reflection toward (**a**) ($\theta_r = 16°$, $\varphi_r = 180°$) (**b**) ($\theta_r = 24°$, $\varphi_r = 45°$) when 2-bit VBCM is encoded by phase gradient coding sequences of [00, 01, 10, 11 …/00, 01, 10, 11 …] and [00, 01, 10, 11 …/01, 10, 11, 00 …/10, 11, 00, 01 …/11, 00, 01, 10 …] respectively. Schematic of 2-bit VBCM driven by [00, 01, 10, 11 …/00, 01, 10, 11 …] and its 3D far-field scattering patterns for (**c**) $M = 3$, (**d**) $M = 6$, (**e**) $M = 7$. (**f**) Theoritical predictions.

creating adjustable pre-defined anomalous reflection driven by the phase-gradient coding sequence. Suppose normally incident wave are illuminating the VBCM structure with phase gradient coding sequences of [00, 01, 10, 11 …/00, 01, 10, 11 …] as shown in Fig. 3(a). According to the generalized Snell's law, the reflection angles θ_r and φ_r can be written as:

$$\theta_r = \arcsin\frac{\lambda}{4MP} \tag{4}$$

$$\varphi_r = \arcsin\frac{\Delta\varphi_y}{\Delta\varphi_x}\frac{D_x}{D_y} \tag{5}$$

where $\Delta\varphi_y$ and $\Delta\varphi_x$ are the phase differences of super-unit-cells along the x- and y- directions, respectively and $D_x = D_y = P$. In the current phase gradient prototype $\Delta\varphi_x = \pi/2$ and $\Delta\varphi_y = 0$, which makes the incident THz wavefront reflected into arbitrary pre-determined oblique angles of ($\theta_r = 16°$, $\varphi_r = 180°$) which are in good agreement with theoretical predictions. To further demonstrate the flexibility of our proposed structure and diverting an impinging wave into a new pre-determined oblique angles of ($\theta_r = 24°$, $\varphi_r = 45°$), a 2-bit VBCM is elaborately encoded exploiting a phase gradient coding sequences of [00, 01, 10, 11 …/01, 10, 11, 00 …/10, 11, 00, 01 …/11, 00, 01, 10 …] leading to $\Delta\varphi_x = \Delta\varphi_y = \pi/2$. The 3D scattered far-field pattern of such encoded metasurface is depicted in Fig. 3(b).

Obviously in anomalous reflection phenomena, by purposefully arranging the coding sequences, the reflected beam can be directed toward a pre-determined azimuth angle in each of four quadrants of ($\varphi_r = 45°$, $135°$, $225°$, $315°$) and at the same frequency, the generated beam elevation angle can be shifted by changing the dimension of lattices of the VBCM structure and beam steering functionality could be envisioned. To validate the concept, the VBCM employed with different size lattices of $M = 3, 6, 7$ are analyzed by the full-wave simulation (see Fig. 3(c–e)) and a good agreement between numerical simulations and theoretical predictions (see Fig. 3(f)) confirm the validity of the presented beam steering analysis in a real-time ultrafast VBCM structure. These examples clearly illustrate that the instantaneous access to an anomalous reflection with outgoing directions is simply realized with our designed VBCM structure. Eventually, by varying the biasing voltage controlled by an FPGA platform, a single beam that can be dynamically altered in pre-determined angles with ultrafast switching time is provided with our presented structure which has fascinating functionality to implement in various applications such as ultrafast THz wireless communications and tracking systems.

multi-beam generation. Recently, it has been revealed that when two different coding patterns are added together through the superposition theorem[112], a combined coding pattern will perform both functionalities simultaneously aid to reach a metasurface with several missions such as multi-beam generation. Two different layouts will be anticipated here to picture the multi-mission capability of the VBCM device. Let us consider two metasurfaces driven by gradient coding sequences along different directions to generate two single beams toward ($\theta_r = 25°$, $\varphi_r = 45°$) and ($\theta_r = 25°$, $\varphi_r = 315°$) respectively. We adopted the superposition theorem here to design a
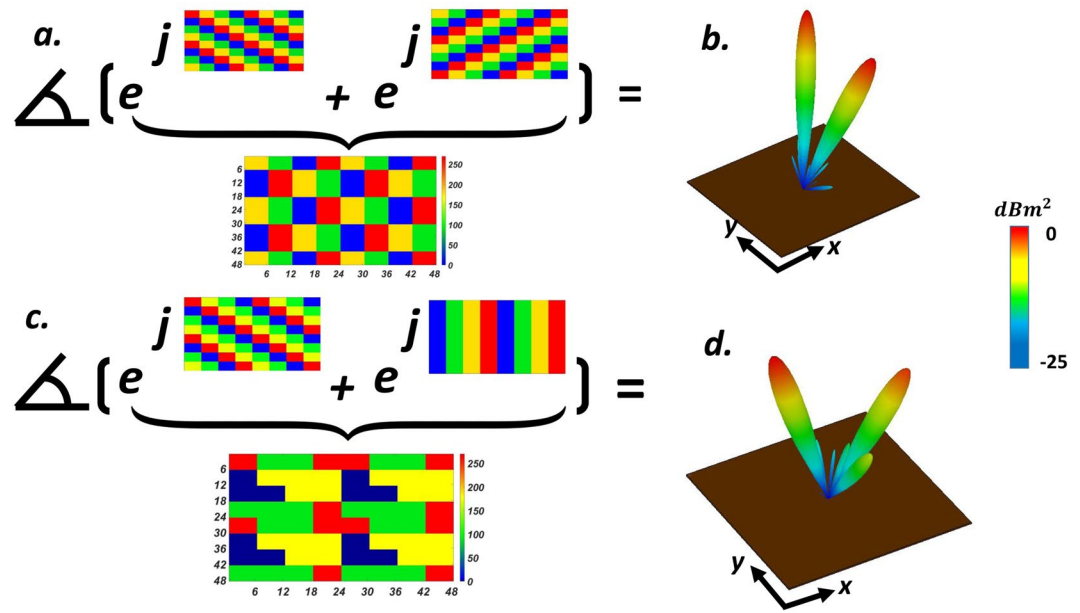
Figure 4. Intuitive display for superposition theorem when two metasurface with gradient coding sequences are added together and two single beams toward (**b**) ($\theta_r = 25°$, $\varphi_r = 45°$, 315°) and (**d**) ($\theta_r = 17°$, $\varphi_r = 180°$), ($\theta_r = 25°$, $\varphi_r = 45°$) are generated successfully. (**a,c**) The initial phase distribution of the metasurfaces before additional operation and the final phase distribution of the mixed metasurface.

2-bit VBCM that redirect the incident THz wavefront from the normal direction into two reflected beams with ($\theta_r = 25°$, $\varphi_r = 45°$, 315°) driven by a coding sequence generated by:

$$(e^{j\varphi_1} + e^{j\varphi_2}) = e^{j\varphi_0} \tag{6}$$

in which φ_1 and φ_2 are arguments of the two primary complex codes and φ_0 represents the argument of superimposed complex code. The 2D phase map of two independent phase gradient metasurface and the final required phase profile of the mixed metasurface to generate proposed multi-beams is depicted in Fig. 4(a) and the 3D scattering pattern of superimposed VBCM is shown in Fig. 4(b). The next example is dedicated to adopting the superposition theorem to add two different gradient coding patterns with distinct elevation angles. Before we delve into the full-wave simulations, it should be noted that when multiple independent pencil beams with different elevation angles are added together, the superimposed coding metasurface generates multiple beams with asymmetric power ratio levels. More recently, by revisiting the addition theorem in the metasurface, our team provided a generalized version of the superposition theorem to estimate the exact amount of power ratio of the multiple beams[113]. Considering the cosine function as the element factor of the metasurface particles, the amount of power distribution of two asymmetric pencil beams can be estimated as follows:

$$\frac{p_{\theta_2}}{p_{\theta_1}} \propto \left[\frac{\cos(\theta_2)}{\cos(\theta_1)} \right]^2 \tag{7}$$

which means that in our designed VBCM structure with two asymmetrically oriented scattering beams, the arbitrarily oriented pencil beam with a higher elevation angle (θ) carrying lower power intensity. Let us consider, two metasurfaces with phase gradient coding sequences one of which makes the incident wave reflect at oblique angles of ($\theta_r = 17°$, $\varphi_r = 180°$) while the other generates single anomalously scattered beam toward ($\theta_r = 25°$, $\varphi_r = 45°$). Exploiting the same design approach results in a VBCM structure that has incorporated both aforesaid gradient codes satisfactorily generates two asymmetrically oriented reflected beams along the pre-determined directions as shown in Fig. 4(d). The initial phase distribution of the metasurfaces before additional operation and the final phase distribution of the mixed metasurface are also provided in Fig. 4(c). Inspired by the addition theorem, these examples proved the correct functioning of our proposed VBCM structure to create symmetric/asymmetric multiple beams in pre-determined directions which is dynamically interchangeable.

Spiral Coding Sequence: vortex beam generation. *Single vortex wavefront carrying different OAM modes.* Since being discovered in 1992[114], vortex beams carrying orbital angular momentum (OAM) has experienced increasing levels of attention for its potential opportunities in high speed communication[115], fast imaging[116], optical manipulation[116], etc. Advantages such as improving the channel capacity without increasing the bandwidth and orthogonality of different topological charges[117] have prompted researchers to present various novel methods for generating vortex beams from spiral phase plates[118] to antenna arrays[119]. However, there are still critical bottlenecks that are waiting for the solutions so that only a few reports involve THz vortex beam
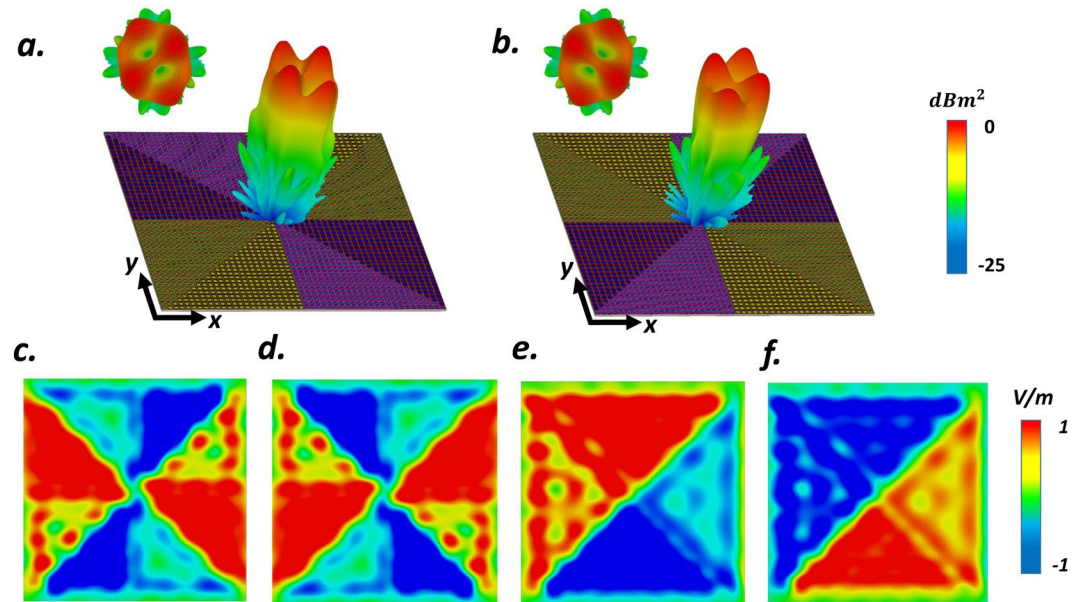
Figure 5. 3D far-field scattering patterns of VBCM structure after dividing the coding mrtasurface into eight segments driven by spiral coding sequences with topological charges of (**a**) $l = +2$ and (**b**) $l = -2$. Simulated y-component of electric field distribution of generated vortex beams with the topological charges of (**c**) $l = +2$; (**d**) $l = -2$; (**e**) $l = +1$ and (**f**) $l = -1$.

realization. Furthermore, future progress in classical and quantum systems requires rapid switch between different OAM modes and at present, they are suffering from lack of ultrafast reconfigurable THz device in order to switch between different OAM modes in a real time-manner.

In order to address the aforesaid restrictions and to further clarify the versatility of our proposed ultrafast tunable VBCM structure, four THz vortex wavefront with different OAM modes ($l = 2, -2, +1, -1$) are envisaged. In each case, the coding metasurface is encoded by a spiral coding sequences generated by:

$$\varphi(x, y) = l \times \arctan\frac{y}{x} \tag{8}$$

In another word, after dividing coding metasurface into N equal segments with phase differences $\Delta\varphi$ of the neighboring segments, the relation between OAM topological charges and the number of segments for our 2-bit coding metasurface yields to:

$$N. \Delta\varphi = 2\pi l \xrightarrow{\Delta\varphi = \frac{\pi}{2}} N = 4l \tag{9}$$

Toward this aim, in order to generate OAM beams with $l = \pm 1$ and $l = \pm 2$, we divided the VBCM structure into four and eight segments with phase shift ranging from 0 to 2π and 0 to 4π respectively. The instant electric field intensities of these four configurations when the observation plane is set as 170 μm away from the center of VBCM structure with an area of 4800 $\mu m \times$ 4800 μm, shown in Fig. 5(c–f). 3D far-field scattering patterns (see Fig. 5(a,b)), demonstrate that the VBCM can successfully generate vortex beams carrying OAM ($l = 2, -2$) at 0.44 THz. According to Fig. 5, a typical doughnut-like intensity profile with an amplitude null in the center (15 dB lower than the annular high-intensity region) satisfies the far-field feature of OAM beams. The capability of ultrafast switching between different topological charges in a real-time manner is provided by our VBCM structure that can empower dramatic advances in wideband OAM based multi-user system where the beams topological charges identify the routing.

Arbitrarily-oriented multiple vortex beams. As a fascinating application in THz OAM-based MIMO systems, generating oriented vortex beam at a predetermined direction which can be dynamically tuned can solve the crucial challenges of this research area. Convolution operation as a simple yet wonderful solution has armed a platform to produce obliquely directed OAM vortex wavefront. Regarding the Fourier transform relation between the coding patterns and its far-field scattering patterns, the scattering pattern shift functionality can be achieved by the means of convolution theorem[120] by adding spiral phase distribution with gradient coding sequences. We start with a simple gradient coding sequence of [00, 01, 10, 11 …/00, 01, 10, 11 …] which generates single anomalously scattered beam toward ($\theta_r = 17°$, $\varphi_r = 180°$). In this example, the OAM-generating spiral-type coding pattern ($l = 1$) is multiplied by the above gradient coding sequence, yielding a tilted vortex scattering pattern along predetermined direction. (see Fig. 6(b,d)). As the next layout, a phase gradient coding sequences of $M_1 = [00, 01, 10, 11 …/01, 10, 11, 00 …/10, 11, 00, 01 …/11, 00, 01, 10 …]$ has added to elaborately encoded four
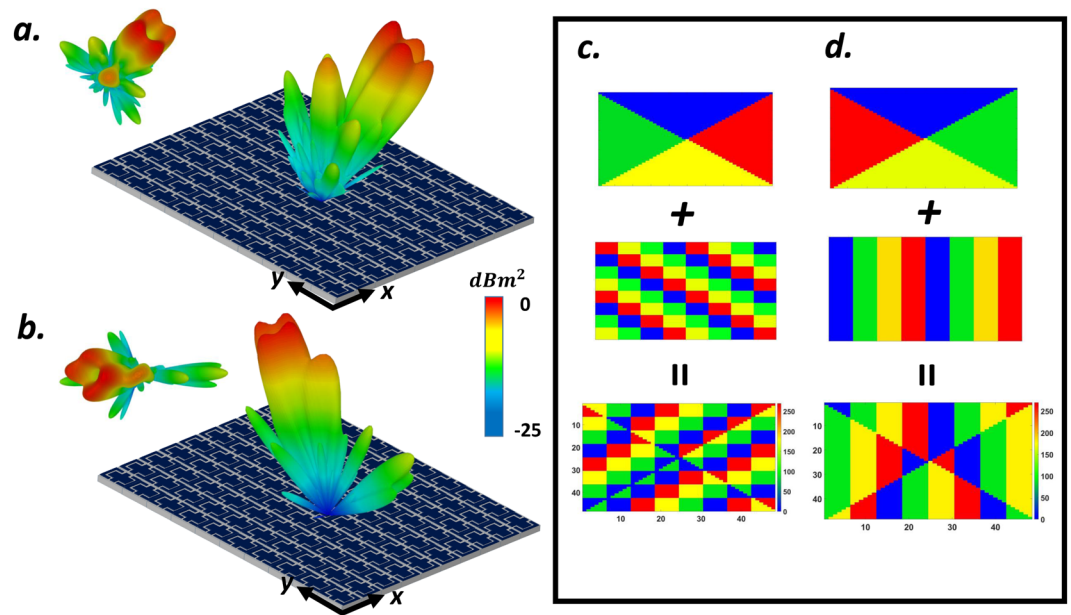
Figure 6. Intuitive display for convolution operation when (**a,c**) spiral coding sequence is added with gradient coding sequence of [00, 01, 10, 11 …/01, 10, 11, 00 …/10, 11, 00, 01 …/11, 00, 01, 10 …] and a tilted-vortex beam is generated toward predetermined direction of ($\theta_r = 25°$, $\varphi_r = 45°$). (**b,d**) Spiral coding sequence is added with gradient coding sequence of [00, 01, 10, 11 …/00, 01, 10, 11 …] to generate oriented-vortex beams toward ($\theta_r = 17°$, $\varphi_r = 180°$).
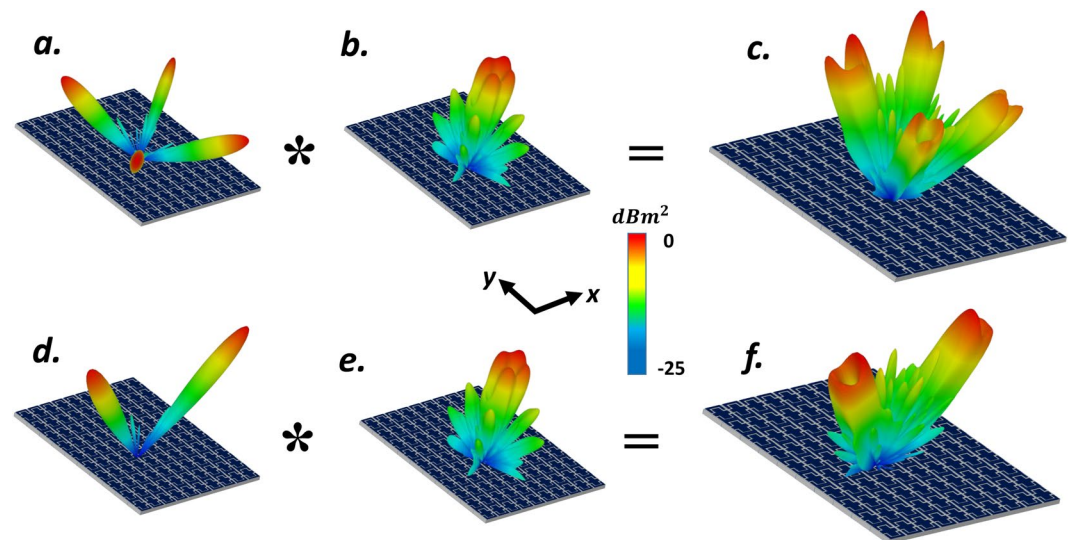

Figure 7. Intuitive presentation of convolution operation on the metasurface levels. (**c,f**) 3D far-field scattering patterns of VBCM structure after multiplying vortex beam with chessboard and stripped configurations respectively. In these two examples we choose (**c**) $M = 10$ and (**f**) $M = 8$ and VBCM structure is occupied with 64×64 and 60×60 unitcells respectively.

segments metasurface with rotated phase distribution ($l = 1$) of M_2 to generate an obliquely directed OAM vortex wavefront in predetermined direction ($M_3 = M_1 + M_2$). The 2D reflection phases map and 3D far-field scattering pattern of such encoded metasurface (M_3) is depicted in Fig. 6(a,c). As can be deduced from Fig. 6, the rotation angle of generated arbitrarily-oriented OAM beam with $l = 1$, which is dictated by the phase gradient coding sequence has good conformity with our theoretical predictions based on Eqs. 4 and 5.

To further specify the ability of the presented structure to generate multiple vortex beams, we add the phase distribution of suitably programmed VBCM to create a vortex beam carrying OAM mode $l = 1$ with a chessboard and stripped configurations respectively. Figure 7(c,f) display the simulated scattering patterns of such encoded metasurfaces after adopting convolution operation. As can be deduced from Fig. 7, the mixed coding patterns
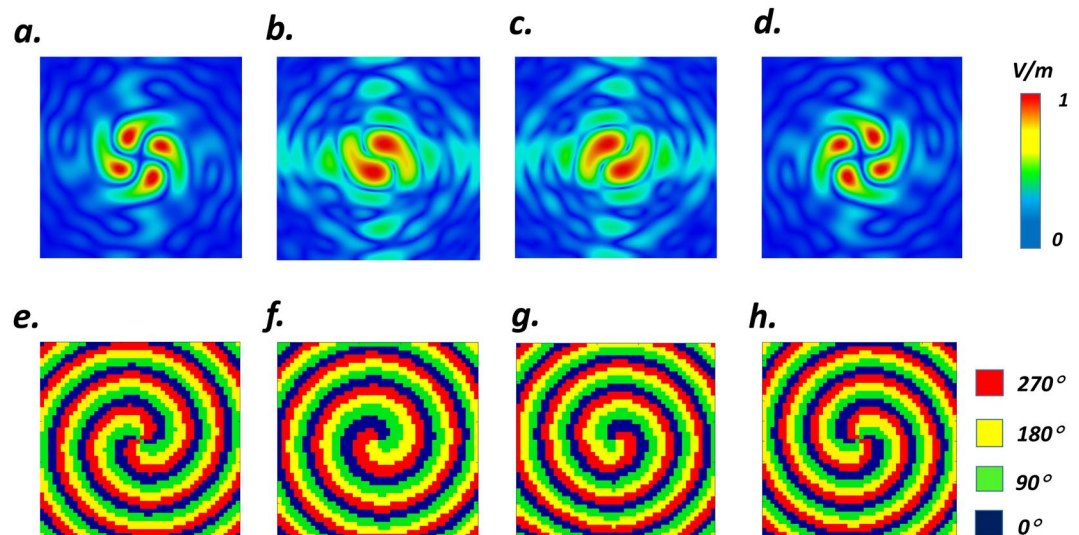
Figure 8. Simulated normalized electric near-field intensities in the sampling planes in xoy plane at different focal distances of (**a**) 1200 μm (**b**) 800 μm (**c**) 1100 μm (**d**) 900 μm corresponding to $l = -2, -1, +1, +2$ respectively. (**e,f**) The required 2D spiral-parabola phase map of VBCM structure to generate different focused vortex beams.

satisfactorily generates four and two symmetrically oriented reflected vortex beams pointing at pre-determined directions of ($\theta_r = 28°$, $\varphi_r = 45°, 135°, 225°, 315°$) and ($\theta_r = 24°$, $\varphi_r = 0°, 180°$) respectively that are very close to our theoretical predictions based on Eqs. 4 and 5. In these two examples we choose $M = 10$ and $M = 8$ and VBCM structure is occupied with 64×64 and 60×60 unitcells respectively. Inspired by the convolution theorem, these examples revealed the competence of our VBCM structure to create arbitrarily-oriented multiple vortex beams in pre-demined directions with different topological charges in a real-time manner.

Focused vortex beam. The versatility of our designed VBCM also has equipped a platform to focus the incident THz wavefront into a pre-determined point. The focal length (Z_{focal}) can be dynamically altered by suitably changed the biasing system of VBCM driven by a parabola phase distribution along the radial direction. Furthermore, our proposed structure provides the ability to obtain several focused vortex beams with ultrafast switching time between different topological charges and focal lengths. To engineer this feature of the work, the phase profile of such encoded VBCM must involve both spiral and parabolic phase distributions simultaneously which can be expressed by[121]:

$$\varphi(x, y) = l \times \arctan\frac{y}{x} + \frac{2\pi}{\lambda}\left(\sqrt{x^2 + y^2 + z_{focal}^2} - z_{focal}\right) \tag{10}$$

To validate the concept, four focused wavefronts carrying OAM with diverse topological charges and focal lengths of $(l, Z_{focal}) = (-1, 800\ \mu m)$, $(l, Z_{focal}) = (-1, 1100\ \mu m)$, $(l, Z_{focal}) = (+2, 900\ \mu m)$ and $(l, Z_{focal}) = (-2, 1200\ \mu m)$ have been designed and exemplified in Fig. 8. In each case, the required 2D spiral-parabola phase map for realizing the corresponding digital states has been pictured in Fig. 8(e–h) respectively. Eventually, illuminating by a y-polarized normal incident plane wave, the focused-vortex-generating VBCM structures are build-up and the simulated normalized electric near-field intensities in the sampling planes at the corresponding focal lengths (see Fig. 8(a–d)) demonstrate the capability and flexibility of the designed VBCM to generate THz focused vortex beams with different OAM modes and focal lengths which is dynamically switchable.

Potential fabrication procedure of the designed structure. In this section, we furnish a brief presentation on the current fabrication technologies[20,122] for fabricating our proposed VO2-based meta atom structure. This process can follow the steps below (see Fig. 9): (a) photoresist is spin-coated and deposited on a substrate using photolithography to form the pattered VO2 bricks; (b) a desired sample pattern is transferred to photoresist by writing the pattern with an electron beam lithography; (c) 1 μm thick VO2 layer is then prepared on 38 μm c-type sapphire substrate using magnetron sputtering technique; (d) lift-off process is adopted in order to dissolve the photoresist and leave behind the film only in the patterned area. Remaining patterned VO2 bricks is annealed at ~450 °C; (e) finally gold layer is deposited on the backside of the substrate as a ground layer. Following the above steps, one can envision a practical fabrication within the scope of the current fabrication technologies.
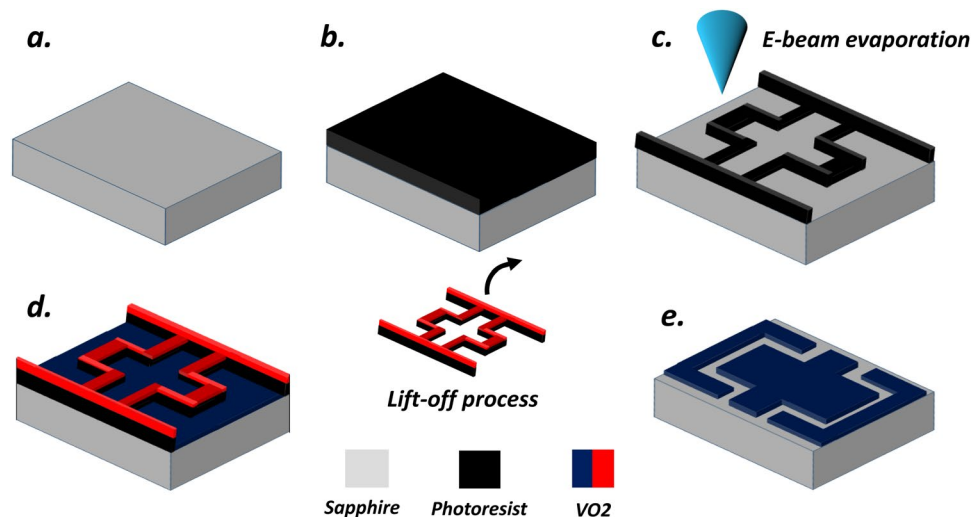
Figure 9. Potential fabrication procedure of the designed structure: (**a**) 38 μm thick *c*-cut sapphire is prepared; (**b**) Photoresist is spin coated and deposited on a substrate using photolithography; (**c**) Photoresist is patterned with an electron beam lithography; (**d**) 1 μm thick VO2 layer is deposited using magnetron sputtered technique; (**e**) lift-off process in order to dissolve the photoresist and final VBCM structure. Remaining patterned VO2 bricks is annealed at 450 °C. Note: VO2 is shown in two different colors (red and blue) just for better visualization.
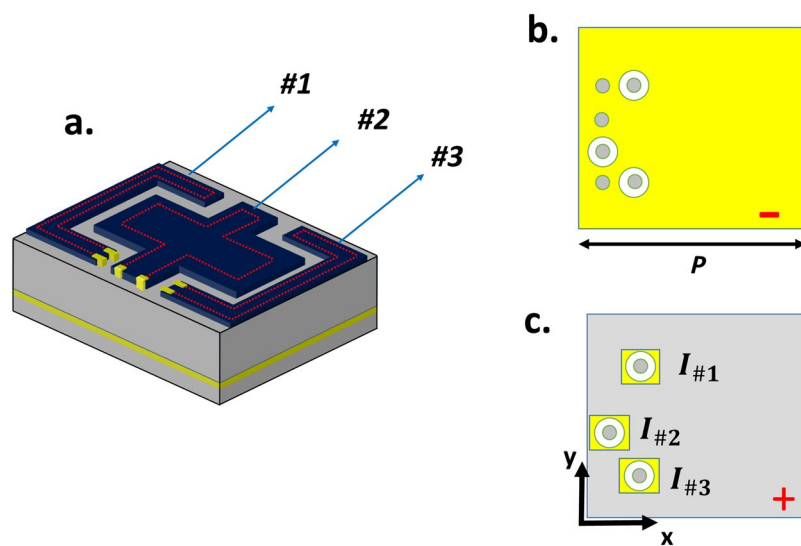

Figure 10. (**a**) Schematic of VBCM integrated with the heater electrode in each patterned film. The two dimensional view (**b**) of the top metallic layer (ground plane) as a negative electrode. (**c**) Three pieces of separated patches on the bottom metallic layer which act as positive electrodes to apply the DC bias current that are electrically isolated from the negative electrode.

Discussion

The necessity of integrating multiple diversified functionalities in a single structure at THz frequencies sparks our curiosity to design a re-programmable multi-mission coding metasurface incorporated with phase-changes materials. In this paper, for the first time, we have proposed a novel reconfigurable metasurface to dynamically manipulate THz wavefront by utilizing the insulator to metal transition of VO2. VO2 thin film exhibits ultrafast switching time which is of great practical significance in ultrafast THz communication. The versatility of our proposed VBCM structure was successfully clarified with different illustrative examples from anomalous reflection to focused vortex beam generation. Furthermore, symmetric/asymmetric multiple beams along the pre-determined directions have also been realized by applying superposition operation. By encoding the VBCM by spiral-like and spiral-parabola-like coding sequences, single vortex beam carrying OAM and focused vortex beam were satisfactorily generated respectively. Additionally, by adopting convolution operation, arbitrarily-oriented multiple vortex beams in pre-determined directions with different topological charges in a real-time manner was realized with

our elaborately designed VBCM. Our ultrafast reconfigurable THz device meets well the THz future industrial demands which require rapidly switch between different OAM modes. In the two last sections, we demonstrated the feasibility of fabricating the VBCM within the realm of the current fabrication technologies and also provided a method for biasing the structure. This simple yet fruitful structure holds great potential for dynamically THz wavefront engineering and can enable advanced applications such as high data rate wireless communication and ultra-massive MIMO communication.

Methods

We used Matlab software version 2016a (https://www.mathworks.com/products/matlab.html) to generate required phase on the surface. All the full-wave numerical simulations are carried out by the means of CST Microwave Studio version 2016 (https://www.3ds.com/products-services/simulia/products/cst-studio-suite/).

The biasing mechanism of the proposed VBCM structure can be realized by photo-induced phase transition for very fast switching time or employing resistive heater electrode for Joule heating actuation. For the sake of briefness, the latter method is only investigated in this section. A resistive heater electrode is placed at the perimeter of the layers to trigger the insulater to metal transition independently for each patterned VO2 film[56] (See Fig. 10(a)). Two thin Au pads are deposited on each patterned VO2 layer which serves as the local bias elements. To apply current to each heating electrode, three metallic via holes are drilled through the top substrate to connect one of the two electrical contacts for each patterned VO2 with the ground layer as a negative electrode. The other three metallics via holes are drilled through the top and bottom substrates to attach other electrical contacts with three pieces of separated patches on the bottom metallic layer which acts as positive electrodes to apply the DC bias current. To ensure that the positive metallic via hole is electrically isolated from the negative electrode (ground plane), a metal ring can be subtracted from the second metallic layer. Figure 10(b,c) shows the two-dimensional view of the top metallic layer (ground plane) as a negative electrode and three pieces of separated patches on the bottom metallic layer which act as positive electrodes to apply the DC bias current. It is important to note that the reflection spectra of the unit-cell is not influenced by adding a new substrate and metallic patches underneath the ground plane. Moreover, very thin heater electrodes and biasing lines with respect to the operating wavelength (analogous to this paper), will not perturb the far-field pattern and therefore have a negligible impact on the macroscopic behavior of our designed VBCM and the individual response of meta-atoms[56,123,124].

References

1. Yang, X. *et al*. Biomedical applications of terahertz spectroscopy and imaging. *Trends Biotechnol.* **34**, 810–824 (2016).
2. Federici, J. & Moeller, L. Review of terahertz and subterahertz wireless communications. *Int. J. Appl. Phys.* **107**, 6 (2010).
3. Kosugi, T., Hirata, A., Nagatsuma, T. & Kado, Y. MM-wave long-range wireless systems. *IEEE Microw. Mag.* **10**, 68–76 (2009).
4. Hirata, A. *et al*. 120-GHz-band millimeter-wave photonic wireless link for 10-Gb/s data transmission. *IEEE Trans Microw Theory tech.* **54**, 1937–1944 (2006).
5. Schurig, D. *et al*. Metamaterial electromagnetic cloak at microwave frequencies. *Science.* **314**, 977–980 (2006).
6. Valentine, J., Li, J., Zentgraf, T., Bartal, G. & Zhang, X. An optical cloak made of dielectrics. *Nat. Mater.* **8**, 568–571 (2009).
7. Smith, D. R., Pendry, J. B. & Wiltshire, M. C. Metamaterials and negative refractive index. *Science.* **305**, 788–792 (2004).
8. Jiang, Z. H. & Werner, D. H. Quasi-three-dimensional angle-tolerant electromagnetic illusion using ultrathin metasurface coatings. *Adv. Funct. Mater.* **24**, 7728–7736 (2014).
9. Pollard, R. J. *et al*. Optical nonlocalities and additional waves in epsilon-near-zero metamaterials. *Phys. Rev. Lett.* **102**, 127405 (2009).
10. Feng, S. & Halterman, K. Coherent perfect absorption in epsilon-near-zero metamaterials. *Phys. Rev. B.* **86**, 165103 (2012).
11. Cui, T. J., Qi, M. Q., Wan, X., Zhao, J. & Cheng, Q. Coding metamaterials, digital metamaterials and programmable metamaterials. *Light Sci. App.* **3**, e218–e218 (2014).
12. Liu, S. & Cui, T. J. Concepts, working principles, and applications of coding and programmable metamaterials. *Adv. Opt. Mater.* **5**, 1700624 (2017).
13. Shabanpour, J. Programmable anisotropic digital metasurface for independent manip- ulation of dual-polarized THz waves based on voltage-controlled phase transition of VO2 microwires. *J. Mater. Chem. C.*, https://doi.org/10.1039/D0TC00689K (2020).
14. Zhang, L., Liu, S., Li, L. & Cui, T. J. Spin-controlled multiple pencil beams and vortex beams with different polarizations generated by Pancharatnam-Berry coding metasurfaces. *ACS Appl. Mater.* **9**, 36447–36455 (2017).
15. Cui, T. J., Liu, S. & Li, L. L. Information entropy of coding metasurface. *Light: Sci. Appl.* **5**, e16172–e16172 (2016).
16. Moeini, M. M., Oraizi, H., Amini, A. & Nayyeri, V. Wide-band beam-scanning by surface wave confinement on leaky wave holograms. *Sci. Rep.* **9**, 1–11 (2019).
17. Moeini, M. M., Oraizi, H. & Amini, A. Collimating cylindrical surface leaky waves for highly improved radiation characteristics of holograms. *Phys. Rev. Appl.* **11**, 044006 (2019).
18. Shao, L., Zhu, W., Leonov, M. Y. & Rukhlenko, I. D. Dielectric 2-bit coding metasurface for electromagnetic wave manipulation. *J. Appl. Phys.* **125**, 203101 (2019).
19. Madni, H. A., Iqbal, S., Liu, S., Zhang, L. & Cui, T. J. Fully-control of OAM vortex beam and realization of retro and negative reflection at oblique incidence using dual-band 2-bit coding metasurface. *arXiv preprint arXiv*:1905.07080 (2019).
20. Li, X. *et al*. Switchable multifunctional terahertz metasurfaces employing vanadium dioxide. *Sci. Rep.* **9**, 1–13 (2019).
21. Wu, P. C. *et al*. Broadband Wide-Angle Multifunctional Polarization Converter via Liquid-Metal-Based Metasurface. *Adv. Opt. Mater.* **5**, 1600938 (2017).
22. Cai, H. *et al*. Multifunctional hybrid metasurfaces for dynamic tuning of terahertz waves. *Adv. Opt. Mater.* **6**, 1800257 (2018).
23. Li, L. *et al*. Intelligent metasurface imager and recognizer. *Light Sci. Appl.* **8**, 1–9 (2019).
24. Li, Y. B. *et al*. Transmission-type 2-bit programmable metasurface for single-sensor and single-frequency microwave imaging. *Sci. Rep.* **6**, 23731 (2016).
25. Ma, Q. *et al*. Smart metasurface with self-adaptively reprogrammable functions. *Light Sci. Appl.* **8**, 1–12 (2019).
26. Li, L. *et al*. Machine-learning reprogrammable metasurface imager. *Nat. Commun.* **10**, 1–8 (2019).
27. Zhang, Q. *et al*. Machine-Learning Designs of Anisotropic Digital Coding Metasurfaces. *Advanced Theory and Simulations.* **2**, 1800132 (2019).

28. Tang, W. *et al*. Wireless communications with programmable metasurface: New paradigms, opportunities, and challenges on transceiver design. *IEEE Wirel. Commun*. (2020).

29. Zhao, J. *et al*. Programmable time-domain digital-coding metasurface for non-linear harmonic manipulation and new wireless communication systems. *Natl. Sci. Rev*. **6**, 231–238 (2019).

30. Tang, W. *et al*. Wireless communications with programmable metasurface: Transceiver design and experimental results. *China. Commun*. **16**(5), 46–61 (2019).

31. Dai, J. Y. *et al*. Wireless communications through a simplified architecture based on time-domain digital coding metasurface. *Adv. Mater. Tech*. **4**, 1900044 (2019).

32. Dai, J. Y. *et al*. Realization of multi-modulation schemes for wireless communication by time-domain digital coding metasurface. *IEEE Trans. Antennas Propag*. (2019).

33. Zhang, L. *et al*. Space-time-coding digital metasurfaces. *Nat. commun*. **9**, 1–11 (2018).

34. Zhang, L. *et al*. Breaking reciprocity with space-time-coding digital metasurfaces. *Adv. Mater*. **31**, 1904069 (2019).

35. Zhang, L., Shao, R., Wu, H. & Cui, T. J. Digital Beam Scanning Technique Based on Space-Time-Modulated Coding Metasurface. In *2019 IEEE MTT-S International Wireless Symposium (IWS)* (pp. 1–3) IEEE (May, 2019).

36. Dai, J. Y., Zhao, J., Cheng, Q. & Cui, T. J. Independent control of harmonic amplitudes and phases via a time-domain digital coding metasurface. *Light Sci. Appl*. **7**, 1–10 (2018).

37. Huang, C. *et al*. Reconfigurable metasurface for multifunctional control of electromagnetic waves. *Adv. Opt. Mater*. **5**, 1700485 (2017).

38. Yang, H. *et al*. A programmable metasurface with dynamic polarization, scattering and focusing control. *Sci. Rep*. **6**, 35692 (2016).

39. Huang, C. *et al*. Dynamical beam manipulation based on 2-bit digitally-controlled coding metasurface. *Sci. Rep*. **7**, 1–8 (2017).

40. Liu, S. *et al*. Full-state controls of terahertz waves using tensor coding metasurfaces. *ACS Appl. Mater*. **9**, 21503–21514 (2017).

41. AbdollahRamezani, S., Arik, K., Farajollahi, S., Khavasi, A. & Kavehvash, Z. Beam manipulating by gate-tunable graphene-based metasurfaces. *Opt. Lett*. **40**, 5383–5386 (2015).

42. Fan, Y., Shen, N. H., Koschny, T. & Soukoulis, C. M. Tunable terahertz meta-surface with graphene cut-wires. *Acs Photonics*. **2**, 151–156 (2015).

43. Fan, Y. *et al*. Tunable mid-infrared coherent perfect absorption in a graphene meta-surface. *Sci. Rep*. **5**, 13956 (2015).

44. Wang, R. *et al*. Triple-band tunable perfect terahertz metamaterial absorber with liquid crystal. *Opt. Express*. **25**, 32280–32289 (2017).

45. He, X. *et al*. Voltage-tunable terahertz metamaterial based on liquid crystal material for bandpass filters and phase shifters. *Integr. Ferroelectrics*. **178**, 131–137 (2017).

46. Du, Y., Tian, H., Cui, X., Wang, H. & Zhou, Z. X. Electrically tunable liquid crystal terahertz phase shifter driven by transparent polymer electrodes. *J. Mater. Chem. C*. **4**, 4138–4142 (2016).

47. Lin, C. J., Li, Y. T., Hsieh, C. F., Pan, R. P. & Pan, C. L. Manipulating terahertz wave by a magnetically tunable liquid crystal phase grating. *Opt. Express*. **16**, 2995–3001 (2008).

48. Chen, A. & Song, Z. Wideband polarization-insensitive dielectric switch for mid-infrared waves realized by phase change material Ge3Sb2Te6. *EPL (Europhysics Letters)* **126**, 27004 (2019).

49. Wei, M., Song, Z., Deng, Y., Liu, Y. & Chen, Q. Large-angle mid-infrared absorption switch enabled by polarization-independent GST metasurfaces. *Mater. Lett*. **236**, 350–353 (2019).

50. Song, Z. & Zhang, J. Achieving broadband absorption and polarization conversion with a vanadium dioxide metasurface in the same terahertz frequencies. *Opt. Express*. **28**, 12487–12497 (2020).

51. Zhang, M. & Song, Z. Terahertz bifunctional absorber based on a graphene-spacer-vanadium dioxide-spacer-metal configuration. *Opt. Express*. **28**, 11780–11788 (2020).

52. Chen, L. & Song, Z. Simultaneous realizations of absorber and transparent conducting metal in a single metamaterial. *Opt. Express*. **28**, 6565–6571 (2020).

53. Song, Z., Chen, A., Zhang, J. & Wang, J. Integrated metamaterial with functionalities of absorption and electromagnetically induced transparency. *Opt. Express*. **27**, 25196–25204 (2019).

54. Makarevich, A. M. *et al*. Chemical synthesis of high quality epitaxial vanadium dioxide films with sharp electrical and optical switch properties. *J. Mater. Chem. C*. **3**, 9197–9205 (2015).

55. Wang, N. *et al*. Mg/W-codoped vanadium dioxide thin films with enhanced visible transmittance and low phase transition temperature. *J. Mater. Chem. C*. **3**, 6771–6777 (2015).

56. Hashemi, M. R. M. *et al*. Electronically-controlled beam-steering through vanadium dioxide metasurfaces. *Sci. Rep*. **6**, 35439 (2016).

57. Wu, S. R., Lai, K. L. & Wang, C. M. Passive temperature control based on a phase change metasurface. *Sci. Rep*. **8**, 1–6 (2018).

58. Coy, H., Cabrera, R., Sepúlveda, N. & Fernández, F. E. Optoelectronic and all-optical multiple memory states in vanadium dioxide. *J. Appl. Phys*. **108**, 113115 (2010).

59. Wen, X. *et al*. Near-infrared active metamaterials and their applications in tunable surface-enhanced Raman scattering. *Opt. Express*. **22**, 2989–2995 (2014).

60. Seo, G., Kim, B. J., Wook Lee, Y. & Kim, H. T. Photo-assisted bistable switching using Mott transition in two-terminal VO2 device. *Appl. Phys. Lett*. **100**, 011908 (2012).

61. Zimmers, A. *et al*. Role of thermal heating on the voltage induced insulator-metal transition in VO 2. *Phys. Rev. Lett*. **110**, 056601 (2013).

62. Shin, J. H., Park, K. H. & Ryu, H. C. Electrically controllable terahertz square-loop metamaterial based on VO2 thin film. *Nanotechnology*. **27**, 195202 (2016).

63. Rathi, S. *et al*. Unravelling the switching mechanisms in electric field induced insulator–metal transitions in VO2 nanobeams. *J. Appl. Phys. D*. **47**, 295101 (2014).

64. Jia, Z. Y. *et al*. Dynamically switching the polarization state of light based on the phase transition of vanadium dioxide. *Phys. Rev. Appl*. **9**, 034009 (2018).

65. Yang, M. *et al*. Suppression of structural phase transition in VO 2 by epitaxial strain in vicinity of metal-insulator transition. *Sci. Rep* **6**, 23119 (2016).

66. Jeong, Y. G., Bahk, Y. M. & Kim, D. S. Dynamic Terahertz Plasmonics Enabled by Phase-Change Materials. *Adv. Opt. Mater*. 1900548 (2019).

67. Cavalleri, A. *et al*. Femtosecond structural dynamics in VO 2 during an ultrafast solid-solid phase transition. *Phys. Rev. Let*. **87**, 237401 (2001).

68. Becker, M. F. *et al*. Femtosecond laser excitation dynamics of the semiconductor-metal phase transition in VO2. *J. Appl Phys*. **79**, 2404–2408 (1996).

69. Cavalleri, A., Dekorsy, T., Chong, H. H., Kieffer, J. C. & Schoenlein, R. W. Evidence for a structurally-driven insulator-to-metal transition in VO 2: A view from the ultrafast timescale. *Phys. Rev. B*. **70**, 161102 (2004).

70. Crunteanu, A. *et al*. Tunable THz metamaterials based on phase-changed materials (VO2) triggered by thermal and electrical stimuli. *In Terahertz, RF, Millimeter, and Submillimeter-Wave Technology and Applications X* (Vol. 10103, p. 101031H) International Society for Optics and Photonics. (February, 2017).

71. Bouyge, D. *et al*. Reconfigurable bandpass filter based on split ring resonators and vanadium dioxide (VO 2) microwave switches. *Asia Pacific Microwave Conference IEEE*. 2332–2335 (December, 2009).
72. Givernaud, J. *et al*. Tunable band stop filters based on metal-insulator transition in vanadium dioxide thin films. 1103–1106 (June, 2008).
73. Earl, S. K. *et al*. Tunable optical antennas enabled by the phase transition in vanadium dioxide. *Opt. Express*. **21**, 27503–27508 (2013).
74. Cormier, P. *et al*. Vanadium dioxide as a material to control light polarization in the visible and near infrared. *Opt. Commun*. **382**, 80–85 (2017).
75. Liang, J., Li, P., Song, X. & Zhou, L. The fabrication and visible–near-infrared optical modulation of vanadium dioxide/silicon dioxide composite photonic crystal structure. *Appl. Phys. A*. **123**, 794 (2017).
76. Nouman, M. T. *et al*. Vanadium dioxide based frequency tunable metasurface filters for realizing reconfigurable terahertz optical phase and polarization control. *Opt. Express*. **26**, 12922–12929 (2018).
77. Born, N. *et al*. Switchable THz Filter Based on a Vanadium Dioxide Layer Inside a Fabry–Pérot Cavity. *IEEE Trans. Terahertz. Sci. Technol*. **5**, 1035–1039 (2015).
78. Zou, H., Xiao, Z., Li, W. & Li, C. Double-use linear polarization convertor using hybrid metamaterial based on VO2 phase transition in the terahertz region. *Appl. Phys. A*. **124**, 322 (2018).
79. Lv, T. T. *et al*. Hybrid metamaterial switching for manipulating chirality based on VO 2 phase transition. *Sci. Rep*. **6**, 23186 (2016).
80. Wu, X., Lan, F., Shi, Z. & Yang, Z. Switchable terahertz polarization conversion via phase-change metasurface. *Progress In Electromagnetics Research Symposium-Spring (PIERS)*. 102–106 (May, 2017).
81. Vegesna, S. *et al*. Terahertz frequency selective surface with reconfigurable polarization characteristics using vanadium dioxide. *J. Electromagnetic. wave*. **28**, 83–90 (2014).
82. Zheng, X., Xiao, Z. & Ling, X. A tunable hybrid metamaterial reflective polarization converter based on vanadium oxide film. *Plasmonics*. **13**, 287–291 (2018). 82.
83. Zhou, G. *et al*. Broadband and high modulation-depth THz modulator using low bias controlled VO 2-integrated metasurface. *Opt. Express*. **25**, 17322–17328 (2017).
84. Han, C., Parrott, E. P., Humbert, G., Crunteanu, A. & Pickwell-Macpherson, E. Broadband modulation of terahertz waves through electrically driven hybrid bowtie antenna-VO 2 devices. *Sci. Rep*. **7**(1), 1–9 (2017).
85. Crunteanu, A. *et al*. Tunable terahertz metamaterials based on metal-insulator phase transition of VO2 layers. *IEEE/MTT-S International Microwave Symposium Digest*. 1–3 (June, 2012).
86. Ding, F., Zhong, S. & Bozhevolnyi, S. I. Vanadium dioxide integrated metasurfaces with switchable functionalities at terahertz frequencies. *Adv. Opt. Mater*. **6**, 1701204 (2018).
87. Zhao, Y., Huang, Q., Cai, H., Lin, X. & Lu, Y. A broadband and switchable VO2-based perfect absorber at the THz frequency. *Opt. Commun*. **426**, 443–449 (2018).
88. Gholamian, M., Shabanpour, J. & Cheldavi, A. Highly sensitive quarter-mode spoof localized plasmonic resonator for dual-detection RF microfluidic chemical sensor. *J. Appl. Phys. Physics. D*. **53**, 145401 (2020).
89. Jeong, Y. G. *et al*. Electrical control of terahertz nano antennas on VO2 thin film. *Opt. Express*. **19**, 21211–21215 (2011).
90. Kim, M., Jeong, J., Poon, J. K. & Eleftheriades, G. V. Vanadium-dioxide-assisted digital optical metasurfaces for dynamic wavefront engineering. *JOSA B*. **33**, 980–988 (2016).
91. Wang, L. *et al*. Reconfigurable multifunctional metasurface hybridized with vanadium dioxide at terahertz frequencies. *Materials*. **11**, 2040 (2018).
92. Wen, Q. Y. *et al*. Terahertz metamaterials with VO2 cut-wires for thermal tunability. *Appl. Phys. Lett*. **97**, 021111 (2010).
93. Xiao, D., Kim, K. W. & Zavada, J. M. Electrically programmable photonic crystal slab based on the metal-insulator transition in VO2. *J. Appl Phys*. **97**, 106102 (2005).
94. Zhang, Y. *et al*. Photoinduced active terahertz metamaterials with nanostructured vanadium dioxide film deposited by sol-gel method. *Opt. Express*. **22**, 11070–11078 (2014).
95. Zhang, H., Jiang, P. & Xu, X. F. Study on a terahertz modulator based on metamaterial with photoinduced vanadium dioxide film. *J. Modern. Opt*. **63**, 1073–1077 (2016).
96. Kim, Y. *et al*. Phase modulation with electrically tunable vanadium dioxide phase-change metasurfaces. *Nano. lett*. **19**, 3961–3968 (2019).
97. Wang, S., Kang, L. & Werner, D. H. Hybrid resonators and highly tunable terahertz metamaterials enabled by vanadium dioxide (VO2). *Sci. Rep*. **7**, 1–8 (2017).
98. Sahana, M. B., Subbanna, G. N. & Shivashankar, S. A. Phase transformation and semiconductor-metal transition in thin films of VO2 deposited by low-pressure metalorganic chemical vapor deposition. *J. Appl. Phys*. **92**, 6495–6504 (2002).
99. Lee, M. H. & Kim, M. G. RTA and stoichiometry effect on the thermochromism of VO2 thin films. *Thin solid films*. **286**, 219–222 (1996).
100. Zhang, H. T. *et al*. Wafer-scale growth of VO2 thin films using a combinatorial approach. *Nat. Commun*. **6**, 8475 (2015).
101. Mandal, P., Speck, A., Ko, C. & Ramanathan, S. Terahertz spectroscopy studies on epitaxial vanadium dioxide thin films across the metal-insulator transition. *Opt. lett*. **36**, 1927–1929 (2011).
102. Fan, F., Hou, Y., Jiang, Z. W., Wang, X. H. & Chang, S. J. Terahertz modulator based on insulator–metal transition in photonic crystal waveguide. *Appl. Opt*. **51**, 4589–4596 (2012).
103. Hashemi, M. R. M., Berry, C. W., Merced, E., Sepúlveda, N. & Jarrahi, M. Direct measurement of vanadium dioxide dielectric properties in W-band. *J Infrared Millim Te* **35**(5), 486–492 (2014).
104. Wang, D. *et al*. Switchable ultrathin quarter-wave plate in terahertz using active phase-change metasurface. *Sci. Rep*. **5**, 1–9 (2015).
105. Radu, I. P. *et al*. Switching mechanism in two-terminal vanadium dioxide devices. *Nano. Technol*. **26**, 165202 (2015).
106. Wu, B. *et al*. Electric-field-driven phase transition in vanadium dioxide. *Phys. Rev. B*. **84**, 241410 (2011).
107. Lee, S. *et al*. Electrically driven phase transition in magnetite nanostructures. *Nat. Mater*. **7**, 130–133 (2008).
108. Joushaghani, A. *et al*. Voltage-controlled switching and thermal effects in VO2 nano-gap junctions. *Appl. Phys. Lett*. **104**, 221904 (2014).
109. Liao, G. M. *et al*. Dynamically tracking the joule heating effect on the voltage induced metal-insulator transition in VO2 crystal film. *AIP Adv*. **6**, 045014 (2016).
110. Yu, N. *et al*. Light propagation with phase discontinuities: generalized laws of reflection and refraction. *Science*. **334**, 333–337 (2011).
111. Nadi, M., Rajabalipanah, H., Cheldavi, A. & Abdolali, A. Flexible Manipulation of Emitting Beams Using Single-Aperture Circularly Polarized Digital Metasurface Antennas: Multi-Beam Radiation toward Vortex-Beam Generation. *Advanced Theory and Simulations*. **3** (2020).
112. Wu, R. Y., Shi, C. B., Liu, S., Wu, W. & Cui, T. J. Addition theorem for digital coding metamaterials. *Adv. Opt. Mater*. **6**, 1701236 (2018).
113. Rajabalipanah, H., Abdolali, A., Shabanpour, J., Momeni, A. & Cheldavi, A. Asymmetric spatial power dividers using phase–amplitude metasurfaces driven by huygens principle. *ACS Omega*. **4**, 14340–14352 (2019).
114. Allen, L., Beijersbergen, M. W., Spreeuw, R. J. C. & Woerdman, J. P. Orbital angular momentum of light and the transformation of Laguerre-Gaussian laser modes. *Phys. Rev. A*. **45**, 8185 (1992).

115. Yan, Y. *et al.* High-capacity millimetre-wave communications with orbital angular momentum multiplexing. *Nat. Commun.* **5**, 1–9 (2014).
116. Liu, K. *et al.* Orbital-angular-momentum-based electromagnetic vortex imaging. *IEEE Antennas Wire. Propag. Lett.* **14**, 711–714 (2014).
117. Zhang, D., Cao, X., Yang, H., Gao, J. & Zhu, X. Multiple OAM vortex beams generation using 1-bit metasurface. *Opt. Express.* **26**, 24804–24815 (2018).
118. Beijersbergen, M. W., Coerwinkel, R. P. C., Kristensen, M. & Woerdman, J. P. Helical-wavefront laser beams produced with a spiral phaseplate. *Opt. Commun.* **112**, 321–327 (1994).
119. Mohammadi, S. M. *et al.* Orbital angular momentum in radio—A system study. *IEEE trans. Antennas Propag.* **58**, 565–572 (2009).
120. Liu, S. *et al.* Convolution operations on coding metasurface to reach flexible and continuous controls of terahertz beams. *Adv. Sci.* **3**, 1600156 (2016).
121. Ma, X. *et al.* A planar chiral meta-surface for optical vortex generation and focusing. *Sci. Rep.* **5**, 10365 (2015).
122. Urade, Y. *et al.* Dynamically Babinet-invertible metasurface: a capacitive-inductive reconfigurable filter for terahertz waves using vanadium-dioxide metal-insulator transition. *Opt. Express* **24**, 4405–4410 (2016).
123. Ma, X. *et al.* An active metamaterial for polarization manipulating. *Adv. Opt. Mater.* **2**, 945–949 (2014).
124. Xu, H. X. *et al.* Dynamical control on helicity of electromagnetic waves by tunable metasurfaces. *Sci. Rep.* **6**, 1–10 (2016).

Author contributions

Javad Shabanpour conceived the idea and designed the VO2-based meta-particle. S. Beyraghi conducted the simulations. Finally, J. Shabanpour wrote the manuscript based on the input from all authors. A. Cheldavi supervised the project and reviewed the manuscript.

Competing interests

The authors declare no competing interests.

Additional information

Correspondence and requests for materials should be addressed to J.S.

Reprints and permissions information is available at www.nature.com/reprints.

Publisher's note Springer Nature remains neutral with regard to jurisdictional claims in published maps and institutional affiliations.